Crystallization process and magnetic properties of amorphous iron oxide nanoparticles



2011 J. Phys. D: Appl. Phys. 44 345002

(http://iopscience.iop.org/0022-3727/44/34/345002)

IOP PUBLISHING JOURNAL OF PHYSICS D: APPLIED PHYSICS

J. Phys. D: Appl. Phys. **44** (2011) 345002 (7pp) doi:10.1088/0022-3727/44/34/345002

# Crystallization process and magnetic properties of amorphous iron oxide nanoparticles

**N D Phu[1], D T Ngo[2], L H Hoang[3], N H Luong[1], N Chau[1] and N H Hai[1]**

[1] Center for Materials Science, Hanoi University of Science, Vietnam National University, Hanoi, 334 Nguyen Trai, Thanh Xuan, Hanoi, Vietnam
[2] Information Storage Materials Laboratory, Toyota Technological Institute, 2-12-1 Hisakata, Tempaku, Nagoya 468-8511, Japan
[3] Faculty of Physics, Hanoi National University of Education, 136 Xuanthuy, Caugiay, Hanoi, Vietnam

E-mail: nhhai@vnu.edu.vn

Received 1 March 2011, in final form 29 June 2011
Published 10 August 2011
Online at stacks.iop.org/JPhysD/44/345002

**Abstract**
This paper studied the crystallization process, phase transition and magnetic properties of amorphous iron oxide nanoparticles prepared by the microwave heating technique. Thermal analysis and magnetodynamics studies revealed many interesting aspects of the amorphous iron oxide nanoparticles. The as-prepared sample was amorphous. Crystallization of the maghemite $\gamma$-$Fe_2O_3$ (with an activation energy of 0.71 eV) and the hematite $\alpha$-$Fe_2O_3$ (with an activation energy of 0.97 eV) phase occurred at around 300 °C and 350 °C, respectively. A transition from the maghemite to the hematite occurred at 500 °C with an activation energy of 1.32 eV. A study of the temperature dependence of magnetization supported the crystallization and the phase transformation. Raman shift at 660 $cm^{-1}$ and absorption band in the infrared spectra at 690 $cm^{-1}$ showed the presence of disorder in the hematite phase on the nanoscale which is supposed to be the origin of the ferromagnetic behaviour of that antiferromagnetic phase.

(Some figures in this article are in colour only in the electronic version)

## 1. Introduction

Iron oxide nanoparticles in crystalline or amorphous state have been used in many applications such as magnetic fluids [1], diagnostic imaging [2], drug delivery [3], biological separation [4], solar energy transformation, magnetic storage media, electronics industry [5] and catalysts [6]. In particular, nm-sized amorphous iron oxide particles have a large surface area therefore they can be a good candidate for gas sorption, sensors and electrode materials [7]. Their disturbed surface structure with a large number of unsaturated bonds endowed them with a high catalytic activity and superparamagnetic behaviour of nanoparticles in colloidal solutions led to their use as magnetic fluids. Moreover, amorphous nanopowder was found to be a suitable precursor for solid-state systems [8].

Many papers have reported on the preparation of iron oxides and their characteristics. There have been a number of studies on the manufacture of crystalline iron oxide nanoparticles such as chemical [9, 10] and physical [1, 11] methods, whereas, there have been only limited studies on the production of amorphous iron oxide nanoparticles because a high cooling rate is required to prepare them. The most common way to obtain amorphous iron oxide nanoparticles is the sonochemical technique [12–14] due to the fact that the cooling rate of this technique can be more than ten million degrees per second [15]. The sonochemical synthetic routes to iron oxides rely on $Fe(CO)_5$ [16, 17], $FeCl_3$ [18], $Fe(NO_3)_3$ [19], $Fe(OAc)_2$ [20] and $Fe(OEt)_3$ [21] as precursors. Other techniques have also been applied to make amorphous iron oxide nanoparticles, such as electrochemical synthesis [22] and microwave heating [23–25]. Microwave heating does not require complicated systems, therefore this technique has attracted more attention of scientists. In microwave heating, microwaves act as high-frequency electric fields and generally heat any material containing mobile electric charges, such as polar molecules in a solvent or conducting ions in a solid. Polar

 

solvents are heated as their component molecules are forced to rotate with the field and lose energy in collisions. Microwave radiation is converted into heat with high efficiency so that superheating becomes possible at ambient pressure, which creates fast homogeneous nucleation of amorphous materials [26, 27].

The crystalline forms of iron (III) oxide can be maghemite ($\gamma$-$Fe_2O_3$) or hematite ($\alpha$-$Fe_2O_3$). Maghemite is ferrimagnetic with a saturation magnetization of 80 emu $g^{-1}$. Hematite has antiferromagnetic properties with a Néel temperature of 680 °C. At room temperature nano-hematite behaves like a weak ferromagnet with a low saturation magnetization of about a few emu $g^{-1}$ [7] or sometimes high saturation magnetization [28]. The origin of the ferromagnetic property of hematite is ascribed to a large number of point defects, or disorders in the material. Hematite possesses a corundum-type structure with the space group $R\bar{3}c$ [28]. An irreversible phase transition from $\gamma$-$Fe_2O_3$ nanoparticles prepared by the gas evaporation method into $\alpha$-$Fe_2O_3$ occurred at 400 °C. For nanocrystalline $\gamma$-$Fe_2O_3$ prepared by the wet chemical method, the reported temperatures of the phase transition to $\alpha$-$Fe_2O_3$ varied in the range 300–500 °C, depending on the experimental method [29, 30]. The origin of the temperature difference is yet unsolved [31].

It is well known that the amorphous state is metastable. It can be transformed to a more stable crystalline state. Amorphous iron oxide nanoparticles prepared by sonochemistry, the microwave heating technique mentioned above, were reported to undergo such amorphous–crystalline transition at a temperature of about 300 °C [24]. A dynamic study of amorphous materials needs information from structural, thermal, spectral and magnetic changes. The dependence of physical properties such as magnetization, structure and thermal properties on the crystallization process is not studied carefully, such as the activation energy and the origin of the ferromagnetic behaviour of hematite. This paper describes the results of the crystallization process, phase transition from the $\gamma$- to the $\alpha$-$Fe_2O_3$ and the origin of the ferromagnetic property of the $\alpha$-phase. Combining the results of structural analysis, temperature dependence of magnetization, time dependence of magnetization, Raman and infrared spectra and differential scanning calorimetry we elucidate the crystallization and magnetodynamics of amorphous iron oxide.

## 2. Experimental

The preparation method chosen was microwave heating which was described earlier with some modifications [24]. A commercial microwave oven (Sanyo 1200 W, Model EM-D9553N) was modified to assist chemical reactions to obtain amorphous iron oxide nanoparticles. Typically, 150 ml solution in a 250 ml flask containing 0.01M ferric chloride $FeCl_3 \cdot 6H_2O$ (Guangdong Chemical, China), 1 wt% percent polyethylene glycol 2000 (Merck) and 1M urea (Xilong Chemical, China) was heated in the oven with a power of 750 W for 15 min. After cooling to room temperature, amorphous iron oxide powder was collected using a centrifuge (Hettich Universal 320, 3500 RPM for 20 min), washed five times with distilled water and air-dried at 75 °C. The final brown product was collected for characterization. The samples were annealed in air using a muffle furnace at temperatures $T_a$ of 200–600 °C for 15 min. The structure of the nanoparticles was analysed using a Bruker D5005 x-ray diffractometer (XRD). The morphology of the materials was examined by a JEM-1200EX transmission electron microscope (TEM) working at an accelerating voltage of 80 kV. Magnetic measurements were conducted using a DMS-880 sample vibrating magnetometer (VSM) with a maximum magnetic field of 13.5 kOe. Thermal behaviour was examined by a STD 2960 TA Instruments differential scanning calorimetry (DSC) over a temperature range 25–750 °C with different heating rates of 5–25 °C $min^{-1}$ under flowing $N_2$ or air. Raman spectra were taken by a Renishaw InVia Raman Micro Raman at room temperature. The samples were excited by the 632.8 nm line from a He–Ne laser with a power level of about 1 mW. Fourier transformed infrared spectra (FTIR) were recorded in the transmission mode on a Nicolet Impact 410 spectrometer.

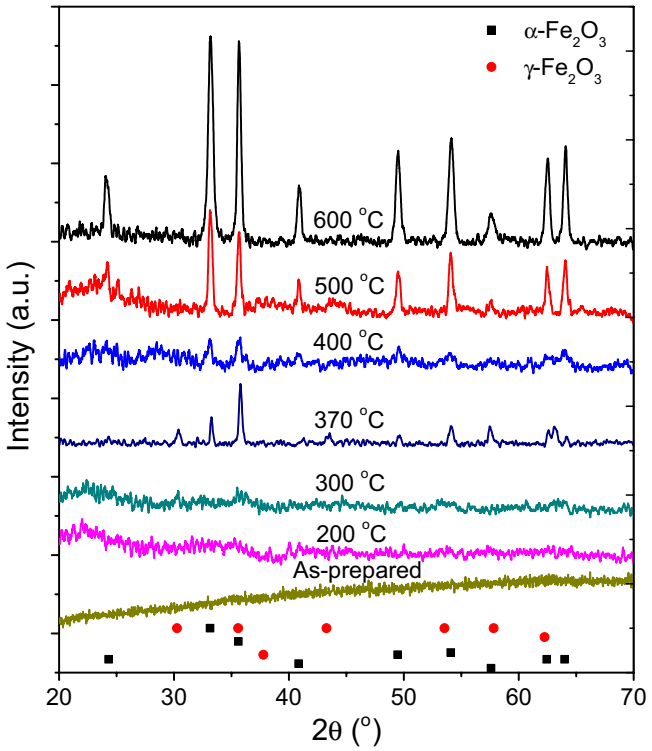


**Figure 1.** XRD patterns of the as-prepared iron oxide nanoparticles and the samples annealed at 200–600 °C.

## 3. Results and discussion

### *3.1. Structure and morphology*

Amorphous behaviour of the as-prepared nanoparticles is shown in the XRD patterns (figure 1) with no significant diffraction peaks. The formation of the amorphous iron oxide nanoparticles in the preparation process is as follows [24]. Polymer $Fe(H_2O)_x(OH^-)_y^{(3-y)+}$, which served as the precursor for the oxide, was formed from complexes of hydrated $Fe^{3+}$ ions with water molecules or $OH^-$ ions.

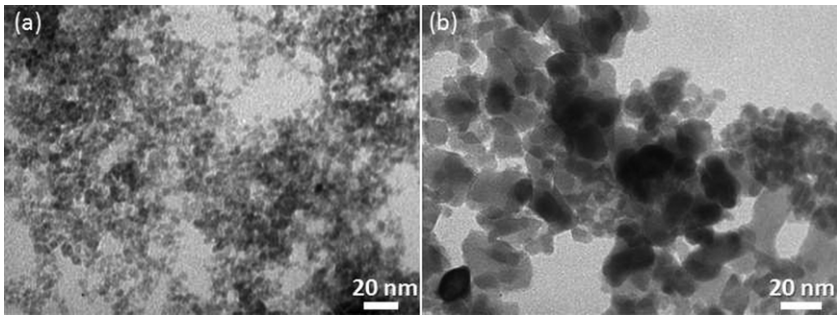


**Figure 2.** TEM images of the as-prepared (*a*) and annealed at 600 °C (*b*) iron oxide nanoparticles.

Fast and homogeneous heating by microwaves stimulated more simultaneous nucleation of iron oxide than heating with conventional methods. Simultaneous nucleation and homogeneous heating can make small particles. In addition, polyethylene glycol, as a dispersion stabilizer, can inhibit non-homogeneous precipitation to obtain homogeneous precipitation. The pH of the solution was adjusted by hydrolysis urea, which is favourable for hydrolysis $Fe^{3+}$ reaction.

Upon annealing at 200 °C, a change in the XRD patterns can be seen but it is hard to identify the exact positions of diffraction peaks. At the annealing temperature of 300 °C, some peaks vaguely appeared at 30.42° and 35.70°, which were assigned to the (2 0 6) and (3 1 3) diffraction planes of the $\gamma$-$Fe_2O_3$ phase, respectively. At higher annealing temperatures of 330 and 350 °C (data not shown), the XRD data were very similar to those of the sample heated at 300 °C. The presence of $\alpha$-$Fe_2O_3$ was not confirmed because the crystallinity of the sample was weak. At 370 and 400 °C, coexistence of maghemite and hematite phases was observed by the presence of diffraction peaks at 30.46° (corresponding to the (2 0 6) plane), 35.84° (3 1 3), 43.47° (0 1 2) and 57.43° (2 1 4) of the $\gamma$-phase and the diffraction peaks at 33.26° (1 0 4), 35.72° (1 1 0) and 49.55° (0 2 4) of the $\alpha$-phase. At annealing temperatures of 500 and 600 °C, the crystallinity of $\alpha$-$Fe_2O_3$ was clear, which was displayed by the strong diffraction peaks of the $\alpha$-$Fe_2O_3$ structure with $R\bar{3}c$ space group. The peaks presented for the $\gamma$-phase, especially the peaks characterized for the (2 0 6) and (0 1 2) planes disappeared when annealed at high temperatures. The intensity of the peaks of the $\alpha$-phase increased with the annealing temperature. The XRD data show that the crystallization of the $\gamma$-phase occurred at around 300 °C. The formation of the $\alpha$-phase happened at 370 and 400 °C. At 500 and 600 °C, the maghemite phase disappeared and there was only $\alpha$-phase in the samples.

Figure 2 is the TEM images of the as-prepared and the annealed at 600 °C iron oxide nanoparticles. The as-prepared amorphous nanoparticles have a size of 3–8 nm. A part of the sample was agglomerates of small particles which may be due to the presence of some remaining chemicals. The annealed sample consists of agglomerates of particles with a diameter of 20–50 nm. The larger size of particles after annealing came from the strong diffusion between nanoparticles at high temperatures.

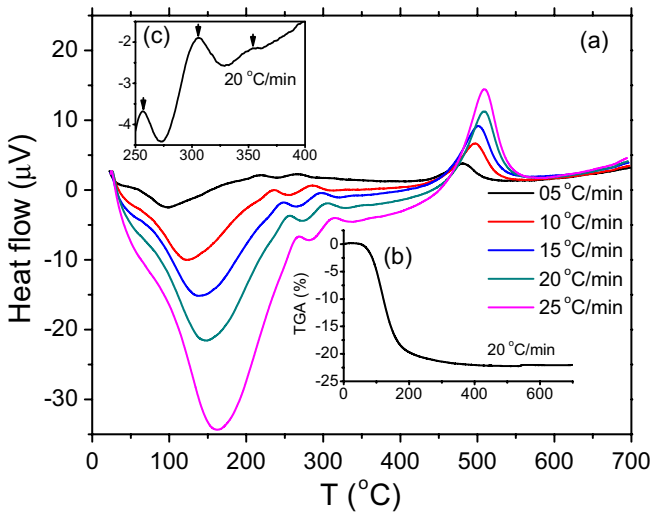


**Figure 3.** DSC results of iron oxide materials with the heating rate $\beta = 5$–$25\ ^\circ\mathrm{C\ min^{-1}}$ (*a*), TGA results (*b*) and a zoom-in of the DSC curve (*c*) with $\beta = 20\ ^\circ\mathrm{C\ min^{-1}}$.

### *3.2. Thermal analysis*

DSC and thermogravimetric analysis (TGA) can be used to measure crystallization and transformation processes. TGA and DSC curves of the iron oxide nanoparticles in air are shown in figure 3. A similarity between our DSC results and previous results [25] was found: except for a slightly different shape of exothermic peaks, no remarkable changes in the heat effects, mass loss and transformation temperatures were observed in argon atmosphere compared with those in air. In figure 3(*a*), all DSC results display a strong endothermic peak located in the range 100–160 °C and four exothermic peaks, located at around 250, 300, 350 and 500 °C. The temperature range of the endothermic peak (figure 3(*b*)) is in the temperature range of the strongest weight loss of TGA results (20 wt%). It can be ascribed to the evaporation of free adsorbed water in the sample. Another 3 wt% loss from 160 to 300 °C may come from the decomposition of residual chemical compounds. At higher temperatures, no significant loss was observed on the TGA curve. In the literature, an exothermic peak at 220 °C was observed from the DSC curve of amorphous iron oxide, which was ascribed to the dehydroxylation of the samples [32]. In our samples, the first exothermic peak located at around 250 °C (position of the peak varied from 220 to 280 °C depending on the heating rate) may be ascribed to this dehydroxylation event

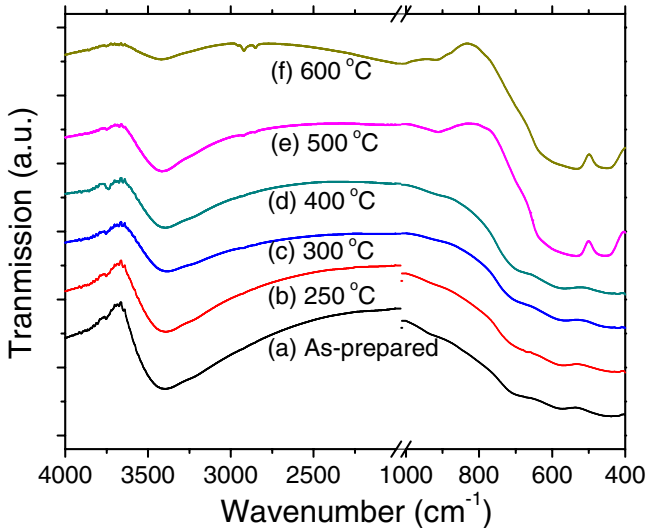


**Figure 4.** FTIR spectra of the as-prepared (*a*) and the samples annealed at 200–600 °C (*b*)–(*f*).

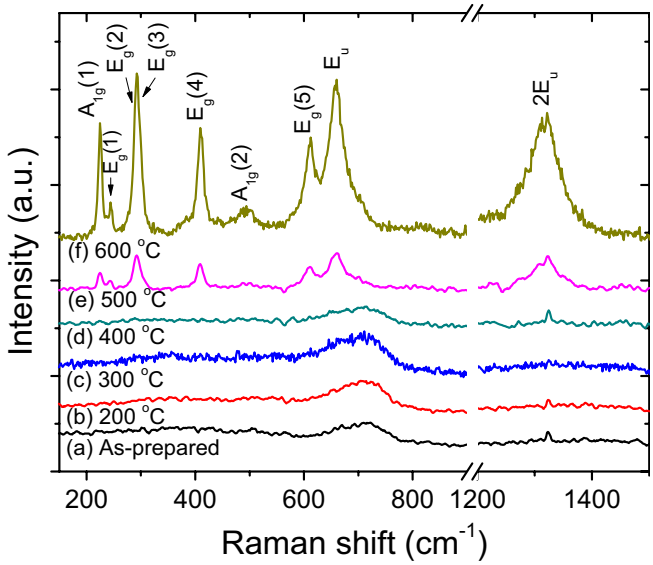


**Figure 5.** Raman shift of the as-prepared (*a*) and the samples annealed at 200–600 °C (*b*)–(*f*).

without changing the structural properties of the materials, which is consistent with the XRD patterns of the samples annealed at 200 °C (figure 1). The second exothermic peak at around 300 °C (265–315 °C) can be due to crystallization of the $\gamma$-$Fe_2O_3$ phase. The presence of maghemite diffraction peaks in the XRD of the samples annealed at 300 °C was supported by the DSC results. The third exothermic peak located at around 350 °C (310–360 °C) is very weak (figure 3(*c*)). In the literature, exothermic peaks at that temperature were ascribed to either the transformation from maghemite to hematite phase or the crystallization of the hematite phase from the amorphous matrix [27]. In our samples, the formation of the maghemite phase already occurred at 300 °C. If the third exothermic peak is due to the phase transformation, this peak should be strong because of the abundance of the maghemite phase. The fact that the third exothermic peak is weak suggests that the this peak is due to the formation of the hematite phase from the remaining amorphous iron oxide materials. This is consistent with the XRD data presented in figure 1 where the coexistence of the maghemite and hematite phases was presented in the samples annealed at 370 and 400 °C. The fourth exothermic peak at around 500 °C (480–510 °C) may be due to the phase transition from the maghemite to the hematite ($\gamma$–$\alpha$) structure. In XRD results (figure 1), the samples annealed at 500 and 600 °C presented only the diffraction peaks from the hematite phase. The crystallization of the $\gamma$ and $\alpha$ phases and the $\gamma$–$\alpha$ transformation have been reported in the literature [29–31]. However, the temperature of crystallization and transformation varied because the activation energy of those processes was low, which made the processes depend strongly on the extrinsic properties.

### *3.3. Raman and infrared spectra study*

Figure 4 presents the room temperature FTIR spectra of the as-prepared and annealed samples. The intensity of the broad peak at about 3400 $cm^{-1}$ corresponding to the H–OH stretch reduces with annealing temperature which can be explained by the evaporation of moieties in the samples. The absorption bands in the range 400–750 $cm^{-1}$, which are characteristic of the Fe–O vibration mode, are present in all the samples [33, 34]. The samples annealed at 400 °C and below are almost the same, which is similar to the behaviour observed in the maghemite material [35]. The absorption bands which were commonly observed in the hematite phase located at 460 and 550 $cm^{-1}$ can be distinguishably seen only in the samples annealed at 500 and 600 °C. Vibration modes of hematite at the Brillouin zone centre are presented by [36]

$$\Gamma = 2A_{1g} + 2A_{1u} + 3A_{2g} + 2A_{2u} + 5E_g + 4E_u.$$

The $A_{1u}$ and $A_{2g}$ modes are optically silent. The symmetrical (g) modes and the asymmetrical (u) modes are active in Raman and infrared spectra, respectively [37]. In the samples annealed at 500 and 600 °C, the absorption band at 550 $cm^{-1}$ corresponded to the overlapped $A_{2u}$ and $E_u$ vibrations, whereas the band at 460 $cm^{-1}$ is due to the $A_{2u}/E_u$ band [7, 38]. In [39], the effect of size dependence on the absorption band in the range 400–750 $cm^{-1}$ was discussed. The small size of the hematite particles led to the broadening of the peak in the range 500–750 $cm^{-1}$. IR transmission spectra of particles with a size of 18 nm (about the size of our sample) in that paper are very similar to the result of our 500 and 600 °C-annealed samples, in which the band at 690 $cm^{-1}$ was assigned to tetrahedral defects of the hematite phase. This suggested that the samples annealed at 500 and 600 °C were hematite with many structural defects.

The Raman spectra of the samples annealed at different temperatures are shown in figure 5. Similar to the XRD data, the Raman modes presented for $\alpha$-$Fe_2O_3$ occurred in the samples annealed at temperatures 500 and 600 °C. Most of the Raman modes presented in figure 5 are in good agreement with the reported Raman spectra of $\alpha$-$Fe_2O_3$ in previous studies [40–43]. Based on previous works, seven Raman active modes occurred in our samples can be assigned as

$A_{1g}$ (225, 494 $cm^{-1}$), $E_g$ (244, 290, 297, 409, 612 $cm^{-1}$) and second harmonic vibration (1320 $cm^{-1}$). It should be noted that a strong mode at 660 $cm^{-1}$ appeared in our result but it is very weak in [40] and ignored in other studies [41–43]. Some works attributed this peak to the existence of the magnetite phase [44, 45]; however, other results [46, 47] showed that this mode is in good agreement with the IR active $E_u$(LO) which is not group-theoretically allowed in Raman spectra. It is reasonable to expect that the mechanism of activation of this mode has arisen originally from the disorder-induced breaking of the symmetry properties of the $E_u$(LO) phonon which may be caused by the defects in the materials. In this case, the disorders may be due to a strong resonance on the surface of the nanoparticles, and the structural defects (for example, oxygen vacancies [48]) formed due to the fast cooling in the preparation process.

### *3.4. Crystallization and phase transition*

The kinetics of the crystallization process in the samples was investigated by studying the DSC signals with different scanning rates. During isothermal transformation, the extent of the crystallization of a certain material is represented by the Johnson–Mehl–Avrami (JMA) equation [49, 50]:

$$x(t) = 1 - \exp(-Kt^n) \tag{1}$$

where $x(t)$ is the volume fraction of the initial material transformed at time $t$, $K$ is the rate constant and $n$ is the order parameter which depends on the mechanism of crystal growth. The rate constant $K$ is given by the Arrhenius equation:

$$K = K_0 \exp\left(-\frac{E_a}{k_B T}\right).$$

In this equation, $E_a$ is the activation energy for the crystallization reaction, which describes the overall crystallization process, $k_B$ is the Boltzmann constant, $T$ is the isothermal temperature and $K_0$ is the frequency factor. Theoretical basis for interpreting the DSC results is the Kissinger model. Studying the shift of the exothermic peaks with different heating rates can provide many interesting insights into the crystallization process [51]. According to the Kissinger model [52], the temperature of the exothermic maximum, $T_{ex}$, is dependent on the heating rate $\beta$ and $E_a$ as follows:

$$\ln\frac{\beta}{T_{ex}^2} = -\frac{E_a}{k_B T_{ex}} + C. \tag{2}$$

The DSC results of iron oxide materials with heating rates of 5–25 °C $min^{-1}$ are given in figure 3. All peaks have a tendency of shifting to a higher temperature as the heating rate is increased. This shift is the result of the fact that the samples have a low thermal conductivity, therefore the temperature of the material at the centre of the samples lagged behind the temperature on the surface. The value of the temperature lag increased with heating rate and made the crystallization process shift to a higher temperature. In addition, the crystallization process is related to the change in molecular mobility, and this mobility has a small time-dependent or kinetic contribution. Fitting the shift of three

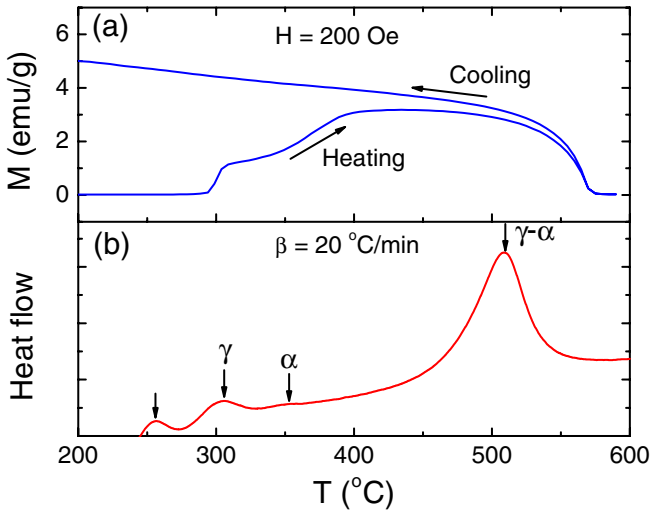


**Figure 6.** Temperature dependence (heating and cooling) of magnetization of the as-prepared iron oxide nanoparticles under a magnetic field of 200 Oe (*a*) compared with the DSC signals with $\beta = 20\,°C\,min^{-1}$ (*b*).

exothermic peaks at around 300, 350 and 500 °C in figure 3 to the linear relationship of the Kissinger equation (2), the obtained activation energies were 0.71 eV, 0.97 eV and 1.32 eV for the $\gamma$-$Fe_2O_3$, $\alpha$-$Fe_2O_3$ crystallization and the $\gamma$–$\alpha$ transformation, respectively. A value of 0.84 eV was reported for the crystallization of $\alpha$-$Fe_2O_3$ prepared by the co-precipitation technique [53], which cannot provide fast cooling in the reaction to obtain the amorphous state of iron oxide. The transformation in that work may be a transition from a non-crystalline iron hydroxide [54] to the $\alpha$-hematite phase, therefore the activation energy is different from the value obtained in this study.

### *3.5. Magnetic properties*

The dependence of magnetization on temperature in a magnetic field of 200 Oe is presented in figure 6. At low temperatures, the heating magnetization is almost zero due to the amorphous state. At high temperatures, the change in magnetization due to the crystallization process is more complicated than a Gaussian-like curve occurring in amorphous ribbons produced by the melt-spinning technique [55]. There were two increases in magnetization at 300 and 360 °C which is ascribed to the crystallization of the $\gamma$-$Fe_2O_3$ and $\alpha$-$Fe_2O_3$ phases, respectively. The first enhancement of magnetization is expected because of the formation of the strongly ferromagnetic maghemite phase. However, we should not expect an increase in magnetization when the maghemite phase is formed. The increase in magnetization when the sample undergoes such an event is due to the ferromagnetic property of the uncompensated antiferromagnet hematite as discussed at the end of the paper. The changes in magnetization are related to the exothermic peaks occurring at 300 and 360 °C in the DSC data (figure 3) and consistent with the XRD data (figure 1) in which only the maghemite and coexistence of the maghemite and the hematite phases was presented in the samples with $T_a = 300$ °C and 370 °C, respectively. The fact

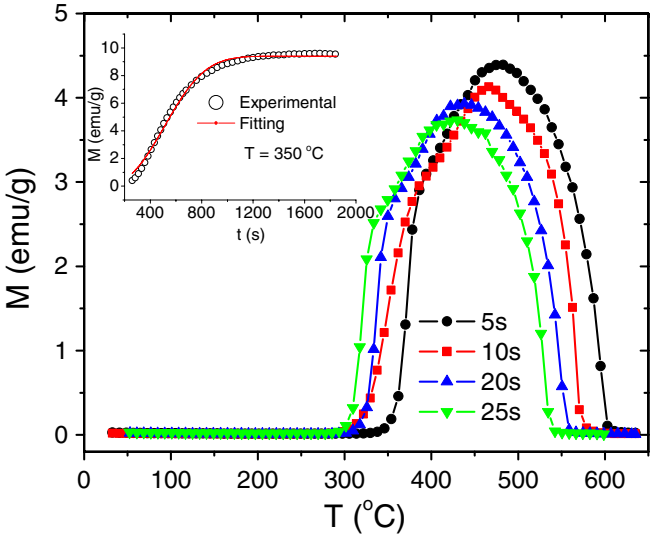


**Figure 7.** The heating magnetization curves under a magnetic field of 20 Oe with different heating rates and the change of magnetization as a function of time at $T = 350\,^{\circ}$C (inset).

that the last exothermic peak related to the $\gamma$–$\alpha$ phase transition did not cause any sudden change in magnetization may be due to the fact that the magnetization of the ferromagnetic maghemite and uncompensated antiferromagnet hematite at high temperatures was not significantly different. The size and agglomeration of particles increased with the heating process. For ferromagnetic materials, this effect can gradually cause an increase in magnetization and cannot result in a sudden change in magnetization.

To check the accuracy of the activation energy for the crystallization process, we used the JMA equation (1) to calculate $E_a$. The volume fraction in that equation was determined from the dependence of magnetization as a function of time $x(t) = M(t)/M_s$, where $M(t)$ is the magnetization at the time $t$, $M_s$ is the saturation magnetization. Writing the JMA equation (1) as $\ln(-\ln(1-x)) = n\ln(K_0 t) - E_a/kT$ and by fitting the magnetization data at 350 °C, near the temperature at which the phase transition occurred, with the JMA equation we obtained the values of the activation energy as 0.76 eV (see the inset in figure 7). $n$ presents the number of dimensions along which nucleation develops. It means that $n = 1$ for 1D growth or surface nucleation; $n = 2$, 3 for 2D and 3D growth, respectively [56]. A value of 2.21 was obtained for $n$ which reveals that the particle growth was not symmetrical in three dimensions. The two values of activation energy for the phase transition obtained from two different ways, i.e. DSC and magnetization, are relatively consistent with each other, which suggests that the values are reasonable. Small values of the activation energy were also observed by ageing the as-prepared sample at room temperature for a few weeks under atmospheric conditions. Therefore, all samples in this study were used for analysis in a few days after preparation.

Figure 7 presents the heating curves of magnetization with different heating rates. We controlled the heating rate by setting a waiting time, $t_{stop}$ of 5–25 s, at each point of measurement as indicated in figure 7. Fast heating corresponds to short values of $t_{stop}$. Similarly to the DSC data, all curves tended to shift to a higher temperature when heated at a higher rate because it had less time at any specific temperature. The temperatures corresponding to the onset of increase in magnetization changed from 300 °C for the waiting time of 5 s to 350 °C for the waiting time of 25 s. Hematite is one antiferromagnetic material in the bulk form [28]. However, ferromagnetic behaviour of the materials at nanosize was reported in many papers [57, 58]. The values of magnetization of our annealed samples are higher than those reported [14] and comparable to the value of hematite with a large number of point defects [28]. The ferromagnetic property of the hematite samples in this paper cannot be related to any phases of Fe, $Fe_3O_4$ and $\gamma$-$Fe_2O_3$. Instead, it can be explained by defects in the $\alpha$-$Fe_2O_3$ materials. The magnetic property of $\alpha$-$Fe_2O_3$ was also investigated both by calculation and experiment, which revealed an increased concentration of oxygen vacancies near the surface [28]. It is reasonable to postulate that these point defects could destroy the antiferromagnetic superexchange interaction of $Fe^{3+}$–$O^{2-}$–$Fe^{3+}$ resulting in an uncompensated antiferromagnetic property and therefore the ferromagnetic behaviour. Ferromagnetic behaviour in hematite was also observed in a sample with a large number of point defects formed because of rapid cooling and heating processes [28]. Similarly to that study, the disorder originated from point defects displayed by the strong $E_u$ mode at 660 $cm^{-1}$ in Raman shift and 690 $cm^{-1}$ in the infrared spectra can be the cause of the ferromagnetic property in our hematite samples.

## 4. Conclusion

Thermal analysis and magnetic study have revealed many interesting aspects of the crystallization of amorphous iron oxide nanoparticles. Activation energies of 0.71 eV, 0.97 eV and 1.32 eV were obtained for the $\gamma$, $\alpha$ phase crystallization and the $\gamma$-$\alpha$ phase transition, respectively. The ferromagnetic property of hematite nanoparticles after annealing at high temperatures can be ascribed to the disorder of the materials on the nanoscale which was confirmed by the study of infrared and Raman spectra. Combining thermal analysis, time dependence magnetic properties and optical spectra is a useful tool for investigating dynamic phenomena in amorphous materials.

## Acknowledgments

This study was financially supported by the National Fund of Science and Technology Development (Nafosted) of Vietnam, Grant 103.02.68.09. The authors would like to thank Dr Nguyen Hoang Nam for experimental help.

## 5. References

[1] Rosenzweig R E 1985 *Ferrohydrodynamics* (Cambridge: Cambridge University Press)
[2] Berry C C and Curtis A S G 2003 *J. Phys. D: Appl. Phys.* **36** R198
[3] Thach C V, Hai N H and Chau N 2008 *J. Korean Phys. Soc.* **52** 1332
[4] Leslie-Pelecky D L, Labhasetwar V and Kraus R H Jr 2005 *Nanobiomagnetics Advanced Magnetic Nanostructures* ed D J Sellmyer and R S Skomski (New York: Kluwer)

[5] Zboril R, Mashlan M and Petridis D 2002 *Chem. Mater.* **14** 969
[6] Li P, Miser D E, Rabiei S, Yadav R T and Hajaligol M R 2003 *Appl. Catal. B-Environ.* **43** 151
[7] Ramesh R, Ashok K, Bhalero G M, Ponnusamy S and Muthamizhchelvan C 2010 *Cryst. Res. Technol.* **45** 965
[8] Schneeweiss O, Zboril R, Pizurova N, Mashlan M, Petrovsky E and Tucek J 2006 *Nanotechnology* **17** 607
[9] Sugimoto T and Matijevic E 1980 *J. Colloid Interface Sci.* **74** 227
[10] Pileni M P 2001 *Adv. Funct. Mater.* **11** 323
[11] Tartaj P, Morales Md P, Veintemillas-Verdaguer S, Gonzalez-Carreno T and Serna C J 2003 *J. Phys. D: Appl. Phys.* **36** R182
[12] Shafi K V P M, Koltypin Y, Gedanken A, Prozorov R, Balogh J, Lendvai J and Felner I 1997 *J. Phys. Chem.* B **101** 6409
[13] Srivastava D N, Perkas N, Gedanken A and Felner I 2002 *J. Phys. Chem.* B **106** 1878
[14] Shafi K V P M, Ulman A, Yan X, Yang N-L, Estournes C, White H and Rafailovich M 2001 *Langmuir* **17** 5093
[15] Suslick K S, Choe S B, Cichowlas A A and Grinstaff M W 1991 *Nature* **353** 414
[16] Cao X, Prozorov R, Koltypin Y, Kataby G, Felner I and Gedanken A 1997 *J. Mater. Res.* **12** 402
[17] Cao X, Koltypin Y, Prozorov R, Kataby G and Gedanken A 1997 *J. Mater. Chem.* **7** 2447
[18] Huang W, Tang X, Felner I, Koltypin Y and Gedanken A 2002 *Mater. Res. Bull.* **37** 1721
[19] Schmidt H 2001 *Appl. Organometall. Chem.* **15** 331
[20] Vijaya Kumar R, Koltypin Y, Xu X N, Yeshurun Y, Gedanken A and Felner I 2001 *J. Appl. Phys.* **89** 6324
[21] Srivastava D N, Perkas N, Zaban A and Gedanken A 2002 *Pure Appl. Chem.* **74** 1509
[22] Pascal C, Pascal J L, Favier F and Moubtassim M L E 1999 *Chem. Mater.* **11** 141
[23] Palchik O, Felner I, Kataby G and Gedanken A 2000 *J. Mater. Res.* **15** 2176
[24] Liao X, Zhu J, Zhong W and Chen H-Y 2001 *Mater. Lett.* **50** 341
[25] Pinkas J, Reichlova V, Zboril R, Moravec Z, Bezdicka P and Matejkova J 2008 *Ultrason. Sonochem.* **15** 257
[26] Rao K J, Vaidhyanathan B, Gaguli M and Ramakrishnan P A 1999 *Chem. Mater.* **11** 882
[27] Machala L, Zboril R and Gedanken A 2007 *J. Phys. Chem.* B **11** 4003
[28] Wu J, Mao S, Ye Z-G, Xie Z and Zheng L 2010 *Appl. Mater. Interfaces* **2** 1561
[29] Schimanke G and Martin M 2000 *Solid State Ion.* **136–137** 1235
[30] Ennas G, Marongiu G, Musinu A, Falqui A, Ballirano P and Caminiti R 1999 *J. Mater. Res.* **14** 1570
[31] Kido O, Higashino Y, Kamitsuji K, Kurumada M, Sato T, Kimura Y, Suzuki H, Saito Y and Kaito C 2004 *J. Phys. Soc. Japan* **73** 2014
[32] Subrt J, Bohacek J, Stengl V, Grygar T and Bezdicka P 1999 *Mater. Res. Bull.* **34** 905
[33] Stuart B 2004 *Infrared Spectroscopy: Fundamentals and Applications* (Chichester: Wiley) p 143
[34] Battisha J K, Afify H H and Ibrahim M 2006 *J. Magn. Magn. Mater.* **306** 211
[35] Osaka T, Matsunaga T, Nakanishi T, Arakaki A, Niwa D and Iida H 2006 *Anal. Bioanal. Chem.* **384** 593
[36] Porto S P S and Krishman R S 1967 *J. Chem. Phys.* **47** 1009
[37] Chamritski I and Burns G 2005 *J. Phys. Chem.* B **109** 4965
[38] Allen G C and Paul M 1995 *Appl. Spectrosc.* **49** 4
[39] Chernyshova I V, Hochella M F Jr and Madden A S 2007 *Phys. Chem. Chem. Phys.* **9** 1736
[40] Legodi M A and de Waal D 2007 *Dyes Pigments* **74** 161
[41] Shebanova O N and Lazor P 2003 *J. Raman Spectrosc.* **34** 845
[42] Massey M J, Baier U, Merlin R and Weber W H 1990 *Phys. Rev.* B **41** 7822
[43] Reddy M V, Yu T, Sow C H, Shen Z X, Lim C T, Rao G V S and Chowdari B V R 2007 *Adv. Funct. Mater.* **17** 2792
[44] Dekker M J 1990 *Geophys. J. Int.* **103** 233
[45] Ozdemir O and Dunlop D J 2000 *Earth Planet. Sci. Lett.* **177** 59
[46] McCarty K F 1988 *Solid State Commun.* **68** 799
[47] de Faria D L A and Lopes F N 2007 *Vib. Spectrosc.* **45** 117
[48] Schoenhalz A L, Arantes J T, Fazzio A and Dalpian G M 2009 *Appl. Phys. Lett.* **94** 162503
[49] Avrami M 1939 *J. Chem. Phys.* **7** 1103
[50] Johnson W A and Mehl R F 1939 *Trans. Am. Inst. Min. (Metall.) Eng.* **135** 416
[51] Gam D T H, The N D, Hai N H, Chau N, Hoa N Q and Mahmud M S 2008 *J. Korean Phys. Soc.* **52** 1423
[52] Kissinger H 1957 *Anal. Chem.* **29** 1702
[53] Chena Y, Li X H, Wu P L, Li W and Zhang X Y 2007 *Mater. Lett.* **61** 1223
[54] Cornell R M, Giovanoli I R and Schneider W 1990 *Clays Clay Miner.* **38** 21
[55] Ngo D-T, Mahmud M S, Hai N H, Duong H G, Nguyen Q H, McVitie S and Chau N 2010 *J. Magn. Magn. Mater.* **322** 342
[56] Heireche L and Belhadji M 2007 *Chalcogen. Lett.* **4** 23
[57] Darezereshki E 2011 *Mater. Lett.* **65** 642
[58] Bang J H and Suslick K S 2007 *J. Am. Chem. Soc.* **129** 2242